Research Article

Nano Research
2023, 16(5): 7974–7981

ISSN 1998-0124 CN 11-5974/O4
https://doi.org/10.1007/s12274-022-5337-8

In-situ electrochemical restructuring of Cu_2BiS_x solid solution into Bi/Cu_xS_y heterointerfaces enabling stabilization intermediates for high-performance CO_2 electroreduction to formate

Xiaofeng Yang[1], Qinru Wang[1], Feiran Chen[1], Hu Zang[1], Changjiang Liu[1], Nan Yu[1], and Baoyou Geng[1,2] (✉)

[1] *College of Chemistry and Materials Science, the Key Laboratory of Electrochemical Clean Energy of Anhui Higher Education Institutes, Anhui Provincial Engineering Laboratory for New-Energy Vehicle Battery Energy-Storage Materials, Anhui Normal University, Wuhu 241002, China*
[2] *Institute of Energy, Hefei Comprehensive National Science Center, Hefei 230031, China*

Received: 30 October 2022 / **Revised:** 15 November 2022 / **Accepted:** 15 November 2022

ABSTRACT

Bismuth-based materials are prevalent catalysts for CO_2 electroreduction to formate, enduring high hydrogen evolution reactions and inadequate activity and stability. Herein, we reveal that *in-situ* electrochemical transformation of Cu_2BiS_x solid solution into Bi/Cu_xS_y heterointerfaces, which can stabilize the intermediates and achieve highly selective and consistent CO_2 electroreduction. It shows over 85% Faraday efficiency (FE) of formate with a potential window of −0.8 to −1.2 V_{RHE} (RHE: reversible hydrogen electrode) and a stability above 90% over 27 h in H-type cell at −0.9 V_{RHE}. It maintains more than 85% of $FE_{formate}$ at the current density of −25 to −200 $mA·cm^{-2}$, and has stability of about 80% of $FE_{formate}$ at least 10 h at −150 $mA·cm^{-2}$ in flow cell. *In-situ* Fourier transform infrared (FT-IR) spectroscopy measurement confirms that the preferred route of catalytic reaction is to generate $*CO_2^-$ and *OCHO intermediates. The density functional theory (DFT) calculations illustrate that heterointerfaces facilitate the prior process of CO_2 to HCOOH through *OCHO by additional Bi hybrid orbitals. This study is expected to open up a new idea for the design of CO_2 electroreduction catalyst.

KEYWORDS

in-situ electrochemical restructuring, heterointerfaces, CO_2 electroreduction, formate, current density

1 Introduction

CO_2 electroreduction (CO_2RR) to high value-added basic organic chemicals and fuels not only promotes the carbon-neutral cycle, but also realizes the storage of renewable electricity, and is considered to be an effective way to reduce the CO_2 content in the atmosphere [1–4]. Among the CO_2 reduction products, formate is one of the most economically viable products across the board of value-added CO_2 electroreduction chemicals, having potential industrial applications as an integral raw material and potential hydrogen storage carrier for fuel cells, pharmaceuticals, chemical synthesis, etc. [5–7]. Therefore, it has attracted tremendous interest and concern leading to the exploitation of functional and high-performance CO_2 reduction catalysts to product formate [8–12].

Bismuth-based catalysts have attracted much attention for CO_2RR to formate due to their unique catalytic performance and superior application potential [13–18]. Although metallic bismuth plays an important role in the reaction, it is limited by low stability and low current density. Most studies focus on bismuth compounds, such as Bi_2S_3, $Bi_2O_2CO_3$, and so on [19, 20]. In particular, by combining with other components to form a heterojunction interface, Bi can obtain electrons from other components, thereby activating the catalytic surface, improving the adsorption and stabilization of intermediates, inhibiting the hydrogen evolution reaction, and improving the catalytic performance [21, 22]. Therefore, the construction of heterointerfaces between Bi and other components, especially elements that can act as electron donors, is of great significance for the preparation of efficient formate electrocatalysts. However, the construction of heterointerfaces remains a challenge due to the differences in composition and structure on both sides of the interface.

Herein, we built a Bi/Cu_xS_y heterointerface through an *in-situ* electrochemical strategy, starting with the precursor of Cu_2BiS_x solid solution obtained by a simple solvothermal method, where the components of the solid solution can be precisely tuned. In the Bi/Cu_xS_y heterogeneous interface, electrons around Cu shift to Bi orbitals, resulting in the reduction of the shielding effect of electrons in the inner layer of the latter, leading to the activation of Bi. The activated Bi is more likely to trap O atoms in the absorbed HCOO* due to its extra hybrid orbital, facilitating the adsorption of H* and HCOO*, thereby reducing the energy of HCOOH formation, resulting in high selectivity for formate and efficient hydrogen suppression. In H-type cells, it exhibits formate Faraday efficiency (FE) above 85% in the potential window of −0.8 to −1.2 V_{RHE} (RHE: reversible hydrogen electrode) and a stability of more than 27 h at a formate FE above 90%. Importantly, it maintains over 85% $FE_{formate}$ at −25 to −200 $mA·cm^{-2}$ in constant current tests and has a stability of approximately 80% $FE_{formate}$ at −150 $mA·cm^{-2}$ for at least 10 h in flow cell. The reaction pathway

Address correspondence to bygeng@mail.ahnu.edu.cn

was explored by capturing intermediates through *in-situ* infrared spectroscopy, confirming that the reaction produces formate by a pathway where the active intermediate is *OCHO. The density functional theory (DFT) theoretical calculations further reveal that the formation of a heterojunction interface accelerates and optimizes the adsorption process of the intermediate *OCHO, leading to a lower *OCHO free energy and facilitating the formation of formate from CO_2. This study provides a forward-looking strategy for the CO_2 electroreduction to high value-added products and suggests promising ideas for the development of other potential heterojunction catalysts.

2 Experimental section

2.1 Materials and chemicals

All materials were purchased commercially without further purification. Bismuth nitrate pentahydrate ($Bi(NO_3)_3{\cdot}5H_2O$, 99.0%), thiourea (CH_4N_2S, 99.0%), copper sulfate trihydrate ($Cu(NO_3)_2{\cdot}3H_2O$, 99.0%), and glycol ($(CH_2OH)_2$, 99.5%) were all purchased from Aladdin Industrial Co., Ltd. Nafion solution (5 wt.%), and Nafion 211 membrane were purchased from Sigma-Aldrich. The deionized (DI) water was produced using a Millipore Milli-Q grade with a resistivity of 18.2 MΩ·cm. All the chemicals were used as received without any further purification.

2.2 Material synthesis

80 mg $Cu(NO_3)_2{\cdot}3H_2O$ and $Bi(NO_3)_3{\cdot}5H_2O$ were added to 15 mL glycol (solution A), while 114 mg thiourea dissolved into deionized water (solution B). After stirring vigorously for 0.5 h simultaneously, solution A was dosed drop by drop into solution B at a rate of 0.5 mL·min^{-1}. Then the mixed solution was stirred for another 1 h to obtain transparent solutions. The contents were then added to a 50 mL polytetrafluoroethylene (PTFE)-lined stainless-steel autoclave which was suitably sealed and maintained at 100 °C for 12 h. The precipitate was collected by centrifugation, followed by washing with ethylene glycol and ethanol after cooling to room temperature, and then dried in vacuum drying equipment overnight. The obtained product mark was Cu_2BiS_x. The processes of synthesis of $CuBiS_x$, Cu_3BiS_x, Bi_2S_3, and CuS were similar to that of Cu_2BiS_x, except that the proportion of metal salts with a total amount of 0.5 mmol changes.

2.3 Material characterization

The samples were characterized by scanning electron microscopy (SEM, Hitachi 8100) with energy-dispersive X-ray analysis spectroscopy (EDX), transmission electron microscopy (TEM, Hitachi HT7700), powder X-ray diffraction (PXRD, Bruker SmartLab 9kw), and X-ray photoelectron spectroscopy (XPS, Thermo Scientific K-Alpha). Vibration pattern capturing of products by Fourier transform infrared (FT-IR) spectrometer (MAGNA-IR750, Nicolet Instrument Co.).

2.4 Preparation of electrodes

In general, 5 mg of catalyst and 20 μL of Nafion solution (5 wt.%) were applied to 1 mL of aqueous ethanol solution (contains 0.5 mL ethanol and 0.5 mL deionized water) and sonicated over 1 h to attain a uniform ink. The catalyst ink was uniformly spread on a piece of cleaned carbon paper to form the electrode with a catalyst loading of ~ 0.5 mg·cm^{-2}.

2.5 Electrochemical measurements

All electrochemical measurements were carried out in a standard three-electrode system, at room temperature in an H-type cell (separated by a Nafion 211 membrane) controlled by a CHI 760E potentiostat (CH instrument, Shanghai, China). Each compartment of the H-cell contained 50 mL of 0.5 M $KHCO_3$ electrolyte. The reference and counter electrodes were Ag/AgCl (in 3 M KCl solution) and Pt, respectively. CO_2 gas (99.999%) was supplied to the electrolyte with a flow rate of 20 mL·min^{-1} in the electrochemical test. The electrochemical measurements in the flow cell were carried out on a CHI 660e with a current amplifier attached. Experiments in a flow cell with gaseous CO_2 located on the backside of the gas diffusion electrode. The cathode and anode liquids (0.5 M $KHCO_3$) were circulated in succession across the cathode and anode chambers by means of a cation exchange membrane (Nafion 211). The cathode was a prepared gas diffusion electrode (GDE, 2 cm × 0.5 cm) and the anode was a platinum sheet (2 cm × 0.5 cm). The potential of the RHE referenced was calculated by the following formula

$$E_{(RHE)} = E_{(Ag/AgCl)} + 0.197 + 0.0591\,pH \quad (1)$$

CO_2 saturated 0.5 M $KHCO_3$ solution at pH 7.2, and all potentials reported herein were vs. RHE. Polarization curves were attained by linear scanning voltammetry (LSV) with a scan rate of 5 mV·s^{-1}, while electrochemical impedance spectroscopy (EIS) measurements were taken over a frequency range of 100 to 0.1 kHz with a 10 mV amplitude. All tests were tested without *IR* compensation.

In-situ attenuated total reflection infrared spectroscopy (ATR-IR) electrochemical tests were performed in a CO_2 saturated 0.5 M $KHCO_3$ electrolyte. We tested the spectrograms of 60 min of sampling every 5 min after 10 min of reaction at different potentials and under −1.0 V_{RHE}, where the wavelength range was 1,000–2,500 cm^{-1}.

The gaseous products of CO_2 electroreduction were monitored in the electrolysis every 30 min via an online gas chromatography (GC, GC9790plus). High purity argon (99.999%) was utilized as the carrier medium. The content of CO was detected by flame ionization detector (FID), installed methane conversion device in front of FID, and detected H_2 content with thermal conductivity detector (TCD). The gas Faraday efficiency was computed by the following equation

$$FE = \frac{npgxF}{RTi} \quad (2)$$

where, n is the reaction electron transfer number, g (mL·min^{-1}) is the CO_2 gas flow rate, x is the gas concentration detected by gas chromatography, $i_{(A)}$ is the total current of the collected gas test, p = 101,325 Pa, F = 96,500 C·mol^{-1}, T = 298.15 K, and R = 8.314 J·mol^{-1}·K^{-1}.

The liquid-phase products were collected and quantified on nuclear magnetic resonance spectroscopy (^{1}H NMR, Bruker ASCEnd TM400) after electrolysis. 500 μL of the reacted electrolyte was then mixed with 100 μL of deuterated dimethyl sulfoxide (where dimethyl sulfoxide was in deuterated water at 100 ppm (v/v)). The following formula was used to calculate the Faraday efficiency of liquid products

$$FE = \frac{n_i z_i F}{It} \quad (3)$$

where n_i is the amount of product in moles, z_i is the number of the transferred electrons, I is the electric current, and t is the total duration of electrolysis.

The partial current density was calculated as follows

$$j_{partial} = j_{total} \times FE \quad (4)$$

where $j_{partial}$ is the partial current density, j_{total} is the total current density, and the FE is the Faraday efficiency of corresponding product.

2.6 Theoretical calculation

The density functional theory calculations were done with the Vienna *ab initio* Simulation Program (VASP). A generalized gradient approximation (GGA) of the type Perdew–Burke–Ernzerhof (PBE) and a 500 eV cut-off energy for the plane wave basis set were introduced. Use 3 × 3 × 1 Monkhorst Pack grid samples Brillouin zone in structural optimization. The interaction between ions and electrons was described by projection enhanced wave (PAW) method. The convergence criterion of structural optimization was that the maximum force on each atom is less than 0.01 eV·Å^{-1}, and energy change was less than 1 × 10^{-5} eV. The DFT-D3 semiempirical correction was described via Grimme's scheme method. Gibbs free energy change of each element step (ΔG) was defined as

$$\Delta G = \Delta E + \Delta \mathrm{ZPE} - T\Delta S + \Delta G_U + \Delta G_{\mathrm{pH}} \quad (5)$$

where, ΔE and ΔZPE are the adsorption energy calculated based on density functional theory and the adsorption energy corrected by zero point energy, respectively. T, ΔS, ΔG_U, and ΔG_{pH} represent the free energy correction values of temperature, entropy change, applied electrode potential, and pH, respectively.

3 Results and discussion

The Cu_2BiS_x solid solution was fabricated through a one-step surfactant-free low temperature solvothermal method using glycol as solvent (Fig. S1 in the Electronic Supplementary Material (ESM)). The XRD patterns of the products with different copper contents are shown in Fig. S2 in the ESM. For comparison, we provide the XRD patterns of pure Bi_2S_3 and CuS, which match the orthorhombic Bi_2S_3 (JCPDS 65-2431) and cobalt CuS (JCPDS 06-0464), respectively (Figs. S3 and S4 in the ESM). Figure S2 in the ESM reveals that when the Cu content is low (Cu to Bi molar ratio is 1:1), the diffraction peaks of Bi_2S_3 are clearly visible. When the molar ratio of copper to bismuth is 2:1, the diffraction peaks of CuS and Bi_2S_3 are obviously weaker and difficult to separate. When the molar ratio of the two reaches 3:1, only one broad diffraction peak appears in the XRD pattern. Obviously, with the increase of Cu content, the intensity of X-ray diffraction peaks of the product decreased, because the periodicity of the crystal structure was affected by the incorporation of Cu, and when enough Cu was added to Bi_2S_3, a homogeneous solid solution was formed.

As shown in Figs. 1(a) and 1(b), the product Cu_2BiS_x is pure and in high yield, with a flower-like morphology composed of a large number of nanorods. The TEM image in Fig. 1(c) shows that the average diameter of the nanorods is about 20 nm. The morphologies of comparative samples are shown in Fig. S5 in the ESM. Pure Bi_2S_3 exhibits compact flower-like morphology assembled by nanorods, while pure CuS has a microspherical morphology. When Cu:Bi = 1:1 or 2:1, the morphology is close to the Bi_2S_3, while when Cu:Bi = 3:1, the Cu_3BiS_x has a cauliflower-like morphology, which is more similar to CuS microspheres. The TEM images in Fig. S6 in the ESM are consistent with the above results. The high-resolution TEM (HRTEM) image of a single nanorod (Fig. 1(d)) shows an interplanar spacing of 0.329 nm, which is slightly larger than the (210) plane of the orthorhombic Bi_2S_3 phase, and no other crystal planes derived from CuS. In addition, some amorphous regions are also found in Fig. 1(d), such as the parts circled by the yellow dotted line. The above characterizations illustrate that copper atoms have entered the Bi_2S_3 lattice, replacing the Bi sites, reducing the crystallinity of the product, and some regions are amorphous. The structure of copper-doped product is significantly different from pure Bi_2S_3, which is highly crystalline with a 0.355 nm interplanar spacing

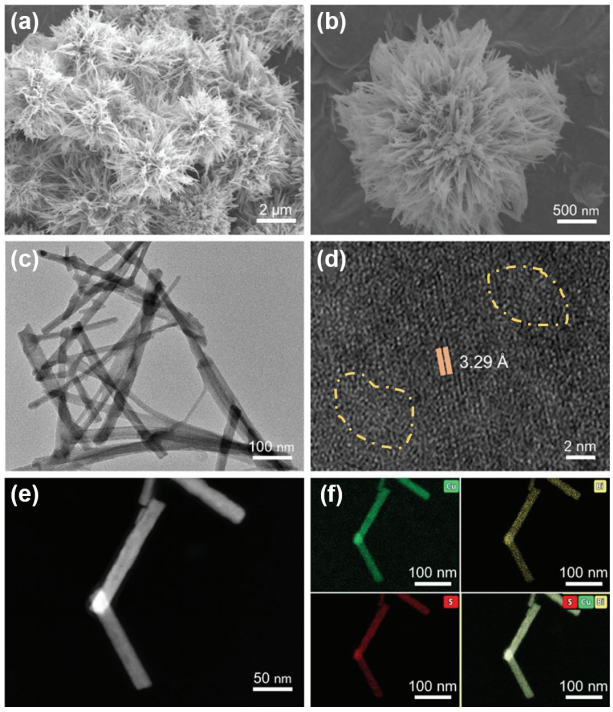

Figure 1 (a) and (b) Low- and high-magnification SEM images, (c) TEM image, (d) HRTEM image, (e) HAADF-STEM image, and (f) corresponding element mappings of Cu_2BiS_x.

corresponding to the Bi_2S_3 (111) plane (Fig. S7 in the ESM). The high-angle annular dark-field scanning TEM (HAADF-STEM) image and corresponding element mappings (Figs. 1(e) and 1(f)) clearly show that the nanorods contain three elements, Cu, Bi, and S, and their distribution is uniform, indicating that the copper is well doped in Bi_2S_3. The EDX element test of the samples shows that the element contents in the products are close to the feeding ratio (Fig. S8 in the ESM).

XPS measurements were performed to reveal the element chemical state on the surface of Cu_2BiS_x. In Fig. S9(a) in the ESM, all diffraction peaks are corrected according to the C 1s peak of 284.9 eV, while the oxygen peak (532.0 eV) can be ascribed to the adsorption of O_2 or H_2O from the atmosphere. Besides, all other peaks correspond well to Cu, Bi, and S elements. Two Cu 2p symmetry peaks (Fig. S9(b) in the ESM) demonstrate the presence of CuS, with binding energies of 932.2 and 952.0 eV for the Cu $2p_{3/2}$ and Cu $2p_{1/2}$ peaks, respectively [23]. As shown in the high-resolution Bi 4f XPS spectrum (Fig. S9(c) in the ESM), two strong peaks at 158.5 and 163.8 eV are assigned to Bi $4f_{7/2}$ and Bi $4f_{5/2}$, respectively, a typical Bi 4f spin-orbit double-peak split of about 5.5 eV for Bi_3^+ signal, while the two weak peaks between them can be assigned to the S 2p signal [24]. In addition, two peaks at 159.5 and 164.8 eV are matched to Bi $4f_{7/2}$ and Bi $4f_{5/2}$ of Bi_2O_3, which show that it is easier to be oxidized when exposed to air than pure Bi_2S_3. Figure S9(d) in the ESM represents the S 2s peak at 225.7 eV ascribable to S_2^-. We investigate the effect of Cu addition on the products by exploring the XPS spectra of each product and binding energy shift of Bi 4f (Figs. S10–S13 in the ESM). The XPS spectra of samples with different Cu contents are almost identical except for minor differences in binding energy, while the XPS spectra of pure Bi_2S_3 and CuS are also consistent with their chemical valence characteristics. With the increase of Cu content, the binding energy of Bi 4f tends to decrease, which is related to electronegativity and element charge. When Bi combines with less electronegative Cu (Cu: 1.36, Bi: 2.02), the electron cloud shifts to the Bi orbital, which gives rise to an extra electron density increase in the outer layer of Bi and reduces the

shielding effect on the inner electrons, thus reducing internal binding energy. The changes of electronic state structure on Bi species are expected to realize the regulation of catalytic performance.

The electrocatalytic performance of the obtained samples for CO_2RR was evaluated in an H-cell with 0.5 M $KHCO_3$ electrolyte. The polarization curves of catalysts in CO_2 or Ar saturated electrolytes can identify whether the material has CO_2RR performance. Therefore, we explored the LSV in distinct gases as depicted in Fig. 2(a), which demonstrated the exclusive electroreduction performance of Cu_2BiS_x due to the lower overpotential and higher current density in the presence of CO_2. The LSV curves of each sample in CO_2-saturated 0.5 M $KHCO_3$ electrolyte are given in Fig. S14 in the ESM. Then, the FE of each product was obtained by chronopotentiometry study and quantitative analysis (Fig. S15 in the ESM). Compared to Bi_2S_3 and other samples, Cu_2BiS_x has lower gas-phase products, especially hydrogen, and has a surprising selectivity for formate from −0.8 to −1.2 V_{RHE}. In addition, it is clear that with the addition of a moderate amount of Cu, the formate selectivity and current density are optimized at Cu:Bi = 2:1 with decent conductivity (Fig. S16 in the ESM). In contrast, the FE of pure CuS is so weak to obtain a good formate selectivity. And remarkably, for Cu_2BiS_x, the FE of formate remains above 85% with a potential window range from −0.8 to −1.2 V_{RHE} under electrochemical measurements, which is much higher than samples with other metal salt ratios, although it has analogous LSV curves with some of them (Fig. 2(b) and Figs. S14 and S15 in the ESM). Formate has always been the dominant product in the testing potential range, retaining over 91% selectivity from −0.8 to −1.0 V_{RHE} and continuing to ascend until slightly reduced on account of competing hydrogen evolution reactions (HER), approaching a partial formate current density at a massive −16.9 mA·cm^{-2} in −1.2 V_{RHE} (Fig. 2(c)). The maximum formate FE of Cu_2BiS_x is up to 93.4% at −0.9 V_{RHE}, while the total FE of its C_1 products reaches 98% in the same potential (Fig. S15 in the ESM). The comparison of the electrocatalytic performance of different samples for CO_2RR to formate is shown in Table S1 in the ESM. The long-term stability testing is another essential metric for measuring CO_2 electroreduction. The stability of the Cu_2BiS_x was evaluated at −0.9 V_{RHE} by chrono-potentiometric electrolysis techniques. Notably, it also exhibited superior and steady $FE_{formate}$ and current density at −0.9 V_{RHE} over 27 h of continuous electrolysis without significant decay (Fig. 2(d)). Performance comparison of Bi-based catalysts in H-type cell is shown in Table S2 in the ESM.

Further, the electrochemical evaluation in the flow cell, a new type of gas-in through substrate (GTS) reactor, greatly improves mass transfer [25, 26]. During electroreduction, cathode solution, anode solution, and gaseous reactants typically flow through three independent chambers of the flow cell, forming a gas–liquid–solid

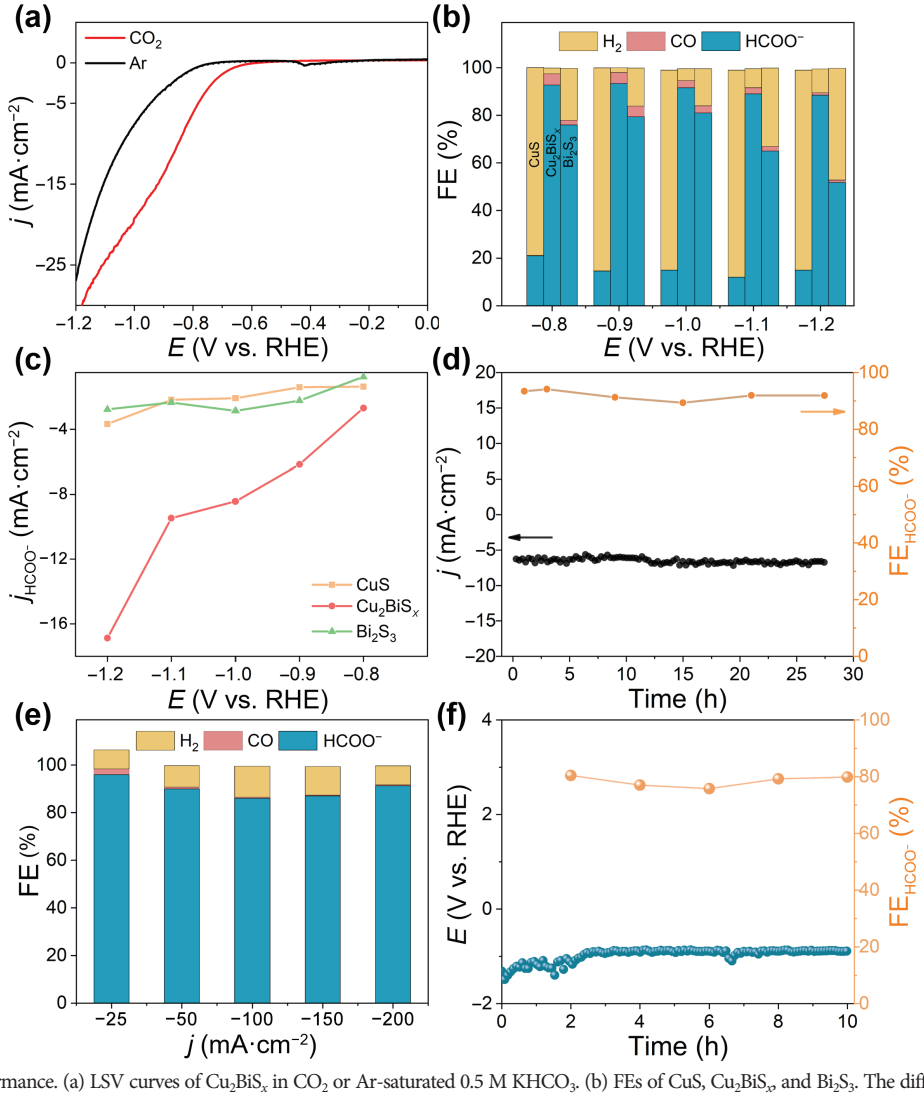

Figure 2 CO_2RR performance. (a) LSV curves of Cu_2BiS_x in CO_2 or Ar-saturated 0.5 M $KHCO_3$. (b) FEs of CuS, Cu_2BiS_x, and Bi_2S_3. The different potentials have the same sequence of samples. (c) Formate current density of CuS, Bi_2S_3, and Cu_2BiS_x. (d) A 100,000 s potentiostat test for the Cu_2BiS_x at −0.9 V_{RHE} in the H-type cell. (e) FEs of Cu_2BiS_x in different current densities. (f) 36,000 s chronopotentiometric test at −150 mA·cm^{-2} in the flow cell.

three-phase interface [27]. Thus, electrochemical investigations with flow cells can achieve significantly higher reaction rates and energy efficiency. Therefore, we further evaluate its CO_2RR performance utilizing the flow cell system in 0.5 M $KHCO_3$ on GDE by LSV and chronopotentiometric measurements, which considerably boost its current density and mass-transfer process. The current density of the catalyst in the CO_2-saturated flow cell is shown in the LSV plots to be well upgraded compared to the Ar atmosphere, demonstrating its good CO_2RR potential (Fig. S17 in the ESM). Furthermore, it is noted in the Fig. 2(e) that the FE of formate retained 85% for Cu_2BiS_x at applied current from −25 to −200 mA·cm^{-2}. In addition, in the 10 h durability test at −150 mA·cm^{-2}, the FE of formate remains around 80%, and the potential is stable (Fig. 2(f)). The performance comparison of Bi based catalyst in flow cell (Table S3 in the ESM) shows the excellent performance of this material, which provides a good potential and important idea for the industrial production of formate in the future [28].

We next investigated the composition and structure evolution of Cu_2BiS_x after electrolysis, revealing its self-regulating state, which is believed to be an important factor in determining the catalyst performance [29]. The TEM and HRTEM images are used to observe the morphology and structure of the product after 20 min (Fig. S18 in the ESM), 1 h (Fig. 3), and 27 h (Fig. S19 in the ESM) of the electrocatalytic reaction (after CO_2RR, Cu_2BiS_x is denoted as R-Cu_2BiS_x). After the reaction, the morphology of the product retains the original nanorod shape, but the size increases and the surface becomes rough (Fig. 3(a)). In the HRTEM image of R-Cu_2BiS_x at 1 h (Fig. 3(b)), crystal regions in different directions can be observed, which are significantly different from the products before electrochemical reaction (Fig. 1(d)). The enlarged HRTEM image (Fig. 3(c)) shows the boundaries, where the crystal planes of 0.237, 0.268, and 0.164 nm can be assigned to Bi (104), Cu_9S_5 (0111), and Cu_9S_8 (204), respectively, proving that the distinct interfaces are formed in the material.

From the HRTEM image after 20 min of reaction (Fig. S18 in the ESM), the material has clearly crystallized, and it can be observed that Cu_9S_5, Cu_9S_8, and Bi crystals have been formed, but they are in different parts and have not yet formed the clear heterogeneous interfaces. At the end of the reaction for 1 h, Bi and Cu_xS_y formed obvious heterointerfaces, and the heterojunction remained until the end of the reaction for 27 h (Fig. S19 in the ESM). The corresponding EDX element mappings show that the three elements Cu, Bi, and S still uniformly distributed on the nanorods, although the crystal structure has completely changed. These results are consistent with the XRD patterns of the R-Cu_2BiS_x at various times (Fig. S20 in the ESM).

Based on the above observation, we deduced the formation mechanism of heterojunctional nanorods. During electrolysis, Bi^{3+} is reduced to elemental Bi, and copper gains electrons to form Cu_xS_y. Elemental Bi combined with Cu_xS_y to form a heterojunction, which stabilized the chemical state of Cu_xS_y (Fig. S21 in the ESM). Namely, through the *in-situ* electrochemical transformation of Cu_2BiS_x, Bi adaptively formed on the heterojunction, which also meant that the highly active Bi sites on the heterojunction remained under the applied electrical potential, thus contributing to the high formate selectivity and stability.

To gain insight into the catalytic reaction pathway of CO_2RR to formate, we utilize *in-situ* ATR-IR to detect the adsorbed species of CO_2 electroreduction through the characteristic absorption of molecular vibrations, aiming to identify key reaction intermediates, thereby determining the preferred reaction pathway for electrocatalysis [30–37]. In particular, a CO_2 saturated 0.5 M $KHCO_3$ electrolyte is added to the special polytetrafluoroethylene electrolytic cell for electrochemical CO_2 reduction of three electrodes, and the *in-situ* infrared technology is used for real-time reaction intermediates monitoring. Firstly, we carried out a real-time analysis of *in-situ* infrared spectroscopy in the range of −0.8 to −1.2 V_{RHE} after electrolysis for 10 min at different negative potentials. From Fig. 4(a), we can visibly follow that the absorption peak at 1,396 cm^{-1} corresponds to the symmetric O–C–O stretching vibration mode of HCOOH and *OCHO, which signifies the formation of formate [38]. *In-situ* IR spectroscopy of electroreduction was undertaken at −1.0 V_{RHE} once every 5 min to derive more comprehensive information about the reaction intermediates and preferential reaction paths. As shown in Fig. 4(b), the distinct absorption peaks correspond to the bands of the specific intermediates. Concretely, the peaks located at 1,726 and 1,290 cm^{-1} correspond to the characteristic bands of *CO_2^-, which also proves the continuous generation of intermediate *CO_2^- with the electrolysis process. In addition, the CO_3^{2-} group appears at 1,477 cm^{-1}, while the asymmetric stretching of the b-CO_3^{2-} group occupies 1,666 cm^{-1}. Therefore, we assert that CO_3^{2-} is formed together when HCO_3^- provides protons

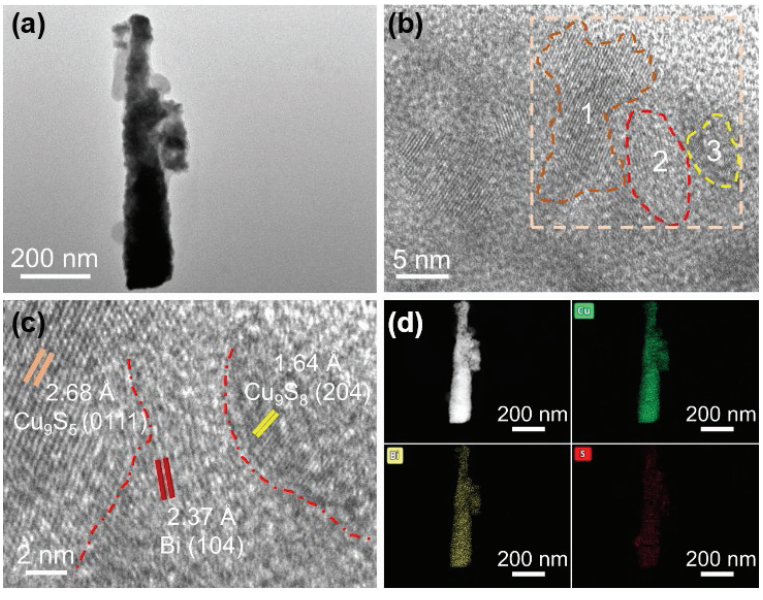

Figure 3 Structural analysis of R-Cu_2BiS_x at 1 h. (a) TEM image, (b) HRTEM image, (c) enlarged HRTEM image, and (d) HAADF-STEM image and corresponding EDX element mappings.

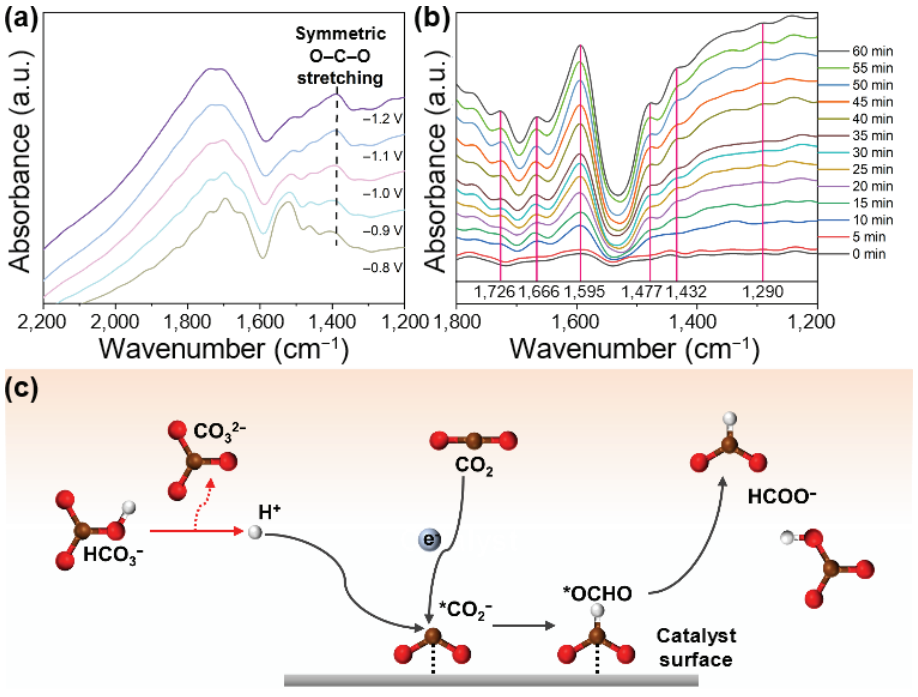

Figure 4 The *in-situ* FT-IR spectra of Cu_2BiS_x. (a) At different voltage after 10 min CO_2RR. (b) At −1.0 V_{RHE} for 60 min potentiostat test. (c) Schematic diagram of priority reaction path.

for intermediates $*CO_2^-$ and *OCHO. The peak at 1,429 cm^{-1} is attributed to the O–C–O symmetric stretching vibrational mode, and its signal intensity gradually enhances with time. In addition, the peak of 1,595 cm^{-1} corresponding to *OCHO has been consistently rising, so it suggests the accumulation of the content of HCOOH and *OCHO.

Based on the above two groups of analysis for the catalytic process corresponding to the *in-situ* IR spectroscopy tests, we can deduce the reaction path of the catalyst Cu_2BiS_x electroreduction of CO_2 to formate with preference as follows

$$CO_2 + * + e^- \rightarrow *CO_2^- \quad (6)$$

$$*CO_2^- + HCO_3^- \rightarrow *OCHO + CO_3^{2-} \quad (7)$$

$$*OCHO + HCO_3^- + e^- \rightarrow HCOOH + CO_3^{2-} \quad (8)$$

We sketched out the reaction path schematic of the overall electrocatalytic procedure to more intuitively and transparently depict the information about the optimal reaction path of catalysis (Fig. 4(c)). It is observed that CO_2 is bound to electrons on the catalyst surface to compose $*CO_2^-$ intermediate, which then combines with HCO_3^- in the electrolyte to formulate *OCHO intermediate, and eventually *OCHO then desorbs by responding with HCO_3^- and electrons to conduce HCOOH.

Further, we explored the reaction paths through DFT calculations to clarify the Gibbs free energies of CO_2RR and HER on the Bi surface, as well as the Bi/Cu_9S_5 and Bi/Cu_9S_8 surfaces, revealing the theoretical reasons for the high selectivity of formate (Figs. S23–S26 in the ESM). The free energies for yielding the HCOOH, CO, and H_2 are given in Figs. 5(a)–5(d) from the DFT studies. The adsorbed *OCHO intermediate in the CO_2RR process is formed by proton–electron transfer, which is the rate-determining step (RDS) for formic acid formation [33]. Meanwhile, CO in CO_2RR is usually formed through carbon-bound intermediates (COOH*), while HER occurs through proton-bound intermediates [35, 39]. Clearly, the Bi/Cu_9S_5 (0.26 eV) and Bi/Cu_9S_8 (0.15 eV) underwent much lower free energies compared to Bi (0.83 eV) for the process of *OCHO to HCOOH, which is the RDS for the HCOOH route. It is shown that the Bi/Cu_9S_5 and Bi/Cu_9S_8 are more likely to boost the formation of HCOOH than Bi. Meanwhile, the Gibbs free energies of CO are 0.72, 0.71, and 0.36 eV on the surface of Bi, Bi/Cu_9S_5, and Bi/Cu_9S_8, indicating that Bi/Cu_9S_8 is more favorable for fostering the formation of CO relative to Bi and Bi/Cu_9S_5 [40]. It further suggests that the contribution of Bi/Cu_9S_8 is greater than that of Bi/Cu_9S_5 when CO is generated on the surface of the heterojunction. In contrast, the Gibbs free energies of H_2 on the surface of Bi, Bi/Cu_9S_5, and Bi/Cu_9S_8 are 0.81, 0.37, and 0.42 eV, respectively, suggesting that the formation of heterojunction makes the *H adsorption stronger, which is conducive to the separation of H_2O and thus effectively inhibits the production of H_2 [41]. However, the free energies of HCOOH are dramatically smaller than that of CO and H_2 on the surface of both Bi/Cu_9S_5 and Bi/Cu_9S_8. Therefore, these results confirm that the Bi/Cu_9S_5 and Bi/Cu_9S_8 heterojunction is more efficient in facilitating the process of CO_2 to HCOOH and in accelerating the kinetics of CO_2.

We also have investigated the electronic interactions between O atoms in adsorbed HCOO* and Bi atoms on the catalyst model surface with the help of projected density of states (PDOS) to reveal further causes for the lowering of energy barriers on heterojunctions. From the calculated results, it can be concluded that the interaction of *OCHO with Bi for each sample is mainly from the s–p orbital hybridization of Bi, and the hybridization regions are mainly distributed in the two light-colored regions (Fig. 5(e)). In contrast, the heterojunctions Bi/Cu_9S_8 and Bi/Cu_9S_5 form red rectangular box wider and more obvious hybridized regions, which are mainly due to Bi p–d orbital hybridization. This additional orbital hybridization enhances the adsorption of the Bi surface to the *OCHO intermediate, stabilizing its state during the reaction and revealing the origin of the fall in the Gibbs free energy of the RDS pathway to HCOOH.

Therefore, the DFT results demonstrate that the Bi atom of monomeric Bi is activated by forming a heterojunction interface with Cu_xS_y. The activated Bi atom is more likely to trap the O atom in the absorbed HCOO*, promoting the binding of H* and HCOO*, and hence reducing the energy of HCOOH formation.

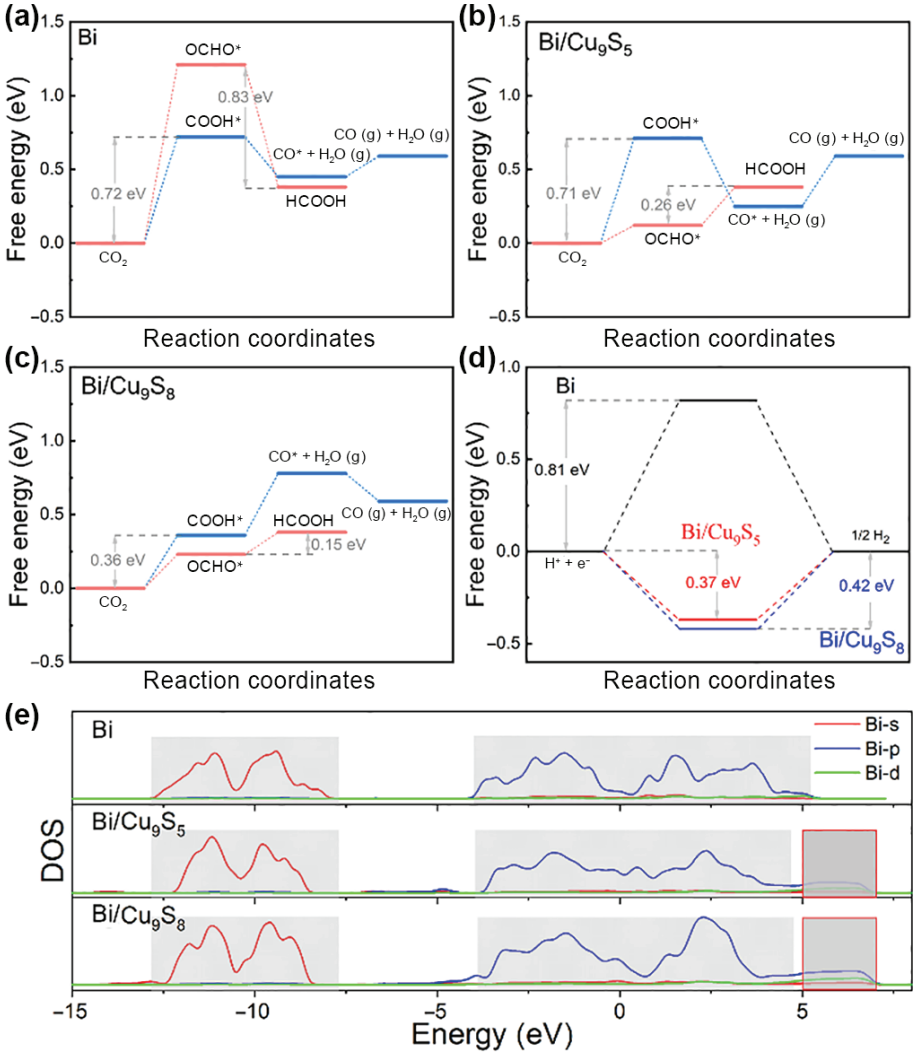

Figure 5 DFT calculation results. (a)–(c) Gibbs free energy diagrams for CO and HCOOH on Bi, Bi/Cu_9S_5, and Bi/Cu_9S_8, respectively. (d) Gibbs free energy diagrams for H_2 on Bi, Bi/Cu_9S_5, and Bi/Cu_9S_8. (e) Projected density of states of s, p, and d orbitals of Bi atom on Bi, Bi/Cu_9S_5, and Bi/Cu_9S_8 surfaces with adsorbed HCOO*.

Thus, we demonstrate that the formation of a heterojunction interface facilitates the kinetics of CO_2 to formate generation by accelerating the adsorption process of the intermediate *OCHO and optimizing it during electrolysis, which in turn leads to a high formate selectivity and stability of the catalyst.

4 Conclusions

In summary, we verify that Cu_2BiS_x solid solution in CO_2RR involves *in-situ* electrochemical transition to catalytically active Bi/Cu_xS_y heterointerfaces during the electrolysis, thus facilitating the yield of formate and long-term stability, repressing the hydrogen evolution reactions. During the reaction, Bi acts as the active site while the addition of Cu adjusts the electronic state by influencing the electronic structure. *In-situ* IR spectroscopy confirms the preferred reaction pathway through the intermediates of $*CO_2^-$ and *OCHO to specifically produce formate. DFT calculations reveal that Cu_9S_5 and Cu_9S_8 consolidate the hybridization orbital of Bi and stabilize the reaction intermediate *OCHO giving it a lower reaction free energy to produce the formate. The strategy of *in-situ* electrochemical construction of heterointerfaces using solid solutions as precursors will inspire the design of efficient and durable electrocatalysts.

Acknowledgements

This work was supported by the National Natural Science Foundation of China (Nos. 21871005 and 22171005) and the University Synergy Innovation Program of Anhui Province (Nos. GXXT-2020-005, GXXT-2021-012, and GXXT-2021-013).

Electronic Supplementary Material: Supplementary material (additional SEM images, TEM images, HAADF-STEM images, XRD patterns, XPS spectra, LSV curves, EIS curves, FEs and partial current densities of formate, CO and H_2, DFT calculation models, and performance comparison in H-type cell and flow cell) is available in the online version of this article at https://doi.org/10.1007/s12274-022-5337-8.

References

[1] Honegger, M.; Michaelowa, A.; Roy, J. Potential implications of carbon dioxide removal for the sustainable development goals. *Climate Policy* **2021**, *21*, 678–698.

[2] Jiang, J. J.; Ye, B.; Liu, J. G. Peak of CO_2 emissions in various sectors and provinces of China: Recent progress and avenues for further research. *Renew. Sust. Energ. Rev.* **2019**, *112*, 813–833.

[3] Koh, L. P.; Zeng, Y. W.; Sarira, T. V.; Siman, K. Carbon prospecting in tropical forests for climate change mitigation. *Nat. Commun.* **2021**, *12*, 1271.

[4] Zeyringer, M.; Price, J.; Fais, B.; Li, P. H.; Sharp, E. Designing low-carbon power systems for Great Britain in 2050 that are robust to the spatiotemporal and inter-annual variability of weather. *Nat. Energy* **2018**, *3*, 395–403.

[5] Liu, X.; Li, S. S.; Liu, Y. M.; Cao, Y. Formic acid: A versatile

renewable reagent for green and sustainable chemical synthesis. *Chin. J. Catal.* **2015**, *36*, 1461–1475.

[6] Pérez-Fortes, M.; Schöneberger, J. C.; Boulamanti, A.; Harrison, G.; Tzimas, E. Formic acid synthesis using CO_2 as raw material: Techno-economic and environmental evaluation and market potential. *Int. J. Hydrogen Energy* **2016**, *41*, 16444–16462.

[7] Zhang, J. W.; Zeng, G. M.; Chen, L. L.; Lai, W. C.; Yuan, Y. L.; Lu, Y. F.; Ma, C.; Zhang, W. H.; Huang, H. W. Tuning the reaction path of CO_2 electroreduction reaction on indium single-atom catalyst: Insights into the active sites. *Nano Res.* **2022**, *15*, 4014–4022.

[8] Chen, S. H.; Li, W. H.; Jiang, W. J.; Yang, J. R.; Zhu, J. X.; Wang, L. Q.; Ou, H. H.; Zhuang, Z. C.; Chen, M. Z.; Sun, X. H. et al. MOF encapsulating N-heterocyclic carbene-ligated copper single-atom site catalyst towards efficient methane electrosynthesis. *Angew. Chem., Int. Ed.* **2022**, *61*, e202114450.

[9] Zhang, X. L.; Zhang, Y.; Li, F. W.; Easton, C. D.; Bond, A. M.; Zhang, J. Ultra-small Cu nanoparticles embedded in N-doped carbon arrays for electrocatalytic CO_2 reduction reaction in dimethylformamide. *Nano Res.* **2018**, *11*, 3678–3690.

[10] Xiao, T. S.; Tang, C.; Li, H. B.; Ye, T.; Ba, K.; Gong, P.; Sun, Z. Z. CO_2 reduction with coin catalyst. *Nano Res.* **2022**, *15*, 3859–3865.

[11] Meng, L. Z.; Zhang, E. H.; Peng, H. Y.; Wang, Y.; Wang, D. S.; Rong, H. P.; Zhang, J. T. Bi/Zn dual single-atom catalysts for electroreduction of CO_2 to syngas. *ChemCatChem* **2022**, *14*, e202101801.

[12] Zhu, Y. T.; Cui, X. Y.; Liu, H. L.; Guo, Z. G.; Dang, Y. F.; Fan, Z. X.; Zhang, Z. C.; Hu, W. P. Tandem catalysis in electrochemical CO_2 reduction reaction. *Nano Res.* **2021**, *14*, 4471–4486.

[13] Zhang, X. L.; Sun, X. H.; Guo, S. X.; Bond, A. M.; Zhang, J. Formation of lattice-dislocated bismuth nanowires on copper foam for enhanced electrocatalytic CO_2 reduction at low overpotential. *Energy Environ. Sci.* **2019**, *12*, 1334–1340.

[14] Zhang, W. J.; Yang, S. Y.; Jiang, M. H.; Hu, Y.; Hu, C. Q.; Zhang, X. L.; Jin, Z. Nanocapillarity and nanoconfinement effects of pipet-like bismuth@carbon nanotubes for highly efficient electrocatalytic CO_2 reduction. *Nano Lett.* **2021**, *21*, 2650–2657.

[15] Wu, D.; Huo, G.; Chen, W. Y.; Fu, X. Z.; Luo, J. L. Boosting formate production at high current density from CO_2 electroreduction on defect-rich hierarchical mesoporous Bi/Bi_2O_3 junction nanosheets. *Appl. Catal. B:Environ.* **2020**, *271*, 118957.

[16] Li, F.; Gu, G. H.; Choi, C.; Kolla, P.; Hong, S.; Wu, T. S.; Soo, Y. L.; Masa, J.; Mukerjee, S.; Jung, Y. et al. Highly stable two-dimensional bismuth metal-organic frameworks for efficient electrochemical reduction of CO_2. *Appl. Catal. B:Environ.* **2020**, *277*, 119241.

[17] Kim, S.; Dong, W. J.; Gim, S.; Sohn, W.; Park, J. Y.; Yoo, C. J.; Jang, H. W.; Lee, J. L. Shape-controlled bismuth nanoflakes as highly selective catalysts for electrochemical carbon dioxide reduction to formate. *Nano Energy* **2017**, *39*, 44–52.

[18] Liu, S. Y.; Hu, B. T.; Zhao, J. K.; Jiang, W. J.; Feng, D. Q.; Zhang, C.; Yao, W. Enhanced electrocatalytic CO_2 reduction of bismuth nanosheets with introducing surface bismuth subcarbonate. *Coatings* **2022**, *12*, 233.

[19] Zhang, Y.; Li, F. W.; Zhang, X. L.; Williams, T.; Easton, C. D.; Bond, A. M.; Zhang, J. Electrochemical reduction of CO_2 on defect-rich Bi derived from Bi_2S_3 with enhanced formate selectivity. *J. Mater. Chem. A* **2018**, *6*, 4714–4720.

[20] Duan, Y. X.; Zhou, Y. T.; Yu, Z.; Liu, D. X.; Wen, Z.; Yan, J. M.; Jiang, Q. Boosting production of HCOOH from CO_2 electroreduction via Bi/CeO_x. *Angew. Chem., Int. Ed.* **2021**, *60*, 8798–8802.

[21] Zhou, J. H.; Yuan, K.; Zhou, L.; Guo, Y.; Luo, M. Y.; Guo, X. Y.; Meng, Q. Y.; Zhang, Y. W. Boosting electrochemical reduction of CO_2 at a low overpotential by amorphous Ag-Bi-S-O decorated Bi^0 nanocrystals. *Angew. Chem., Int. Ed.* **2019**, *58*, 14197–14201.

[22] Yu, J. G.; Zhang, J.; Liu, S. W. Ion-exchange synthesis and enhanced visible-light photoactivity of CuS/ZnS nanocomposite hollow spheres. *J. Phys. Chem. C* **2010**, *114*, 13642–13649.

[23] Tian, L.; Tan, H. Y.; Vittal, J. J. Morphology-controlled synthesis of Bi_2S_3 nanomaterials via single- and multiple-source approaches. *Cryst. Growth Des.* **2008**, *8*, 734–738.

[24] Lv, J. J.; Yin, R. N.; Zhou, L. M.; Li, J.; Kikas, R.; Xu, T.; Wang, Z. J.; Jin, H. L.; Wang, X.; Wang, S. Microenvironment engineering for the electrocatalytic CO_2 reduction reaction. *Angew. Chem., Int. Ed.* **2022**, *134*, e202207252.

[25] Weekes, D. M.; Salvatore, D. A.; Reyes, A.; Huang, A. X.; Berlinguette, C. P. Electrolytic CO_2 reduction in a flow cell. *Acc. Chem. Res.* **2018**, *51*, 910–918.

[26] Endrődi, B.; Samu, A.; Kecsenovity, E.; Halmágyi, T.; Sebők, D.; Janáky, C. Operando cathode activation with alkali metal cations for high current density operation of water-fed zero-gap carbon dioxide electrolysers. *Nat. Energy* **2021**, *6*, 439–448.

[27] Chen, C.; Khosrowabadi Kotyk, J. F.; Sheehan, S. W. Progress toward commercial application of electrochemical carbon dioxide reduction. *Chem* **2018**, *4*, 2571–2586.

[28] Wang, W. B.; Wang, Z. T.; Yang, R. O.; Duan, J. Y.; Liu, Y. W.; Nie, A. M.; Li, H. Q.; Xia, B. Y.; Zhai, T. Y. *In situ* phase separation into coupled interfaces for promoting CO_2 electroreduction to formate over a wide potential window. *Angew. Chem., Int. Ed.* **2021**, *60*, 22940–22947.

[29] Baruch, M. F.; Pander III, J. E.; White, J. L.; Bocarsly, A. B. Mechanistic insights into the reduction of CO_2 on tin electrodes using *in situ* ATR-IR spectroscopy. *ACS Catal.* **2015**, *5*, 3148–3156.

[30] Chen, S.; Chen, A. C. Electrochemical reduction of carbon dioxide on Au nanoparticles: An *in situ* FTIR study. *J. Phys. Chem. C* **2019**, *123*, 23898–23906.

[31] Dutta, A.; Kuzume, A.; Rahaman, M.; Vesztergom, S.; Broekmann, P. Monitoring the chemical state of catalysts for CO_2 electroreduction: An in operando study. *ACS Catal.* **2015**, *5*, 7498–7502.

[32] Feaster, J. T.; Shi, C.; Cave, E. R.; Hatsukade, T.; Abram, D. N.; Kuhl, K. P.; Hahn, C.; Nørskov, J. K.; Jaramillo, T. F. Understanding selectivity for the electrochemical reduction of carbon dioxide to formic acid and carbon monoxide on metal electrodes. *ACS Catal.* **2017**, *7*, 4822–4827.

[33] Firet, N. J.; Smith, W. A. Probing the reaction mechanism of CO_2 electroreduction over Ag films via operando infrared spectroscopy. *ACS Catal.* **2017**, *7*, 606–612.

[34] Katayama, Y.; Nattino, F.; Giordano, L.; Hwang, J.; Rao, R. R.; Andreussi, O.; Marzari, N.; Shao-Horn, Y. An *in situ* surface-enhanced infrared absorption spectroscopy study of electrochemical CO_2 reduction: Selectivity dependence on surface C-bound and O-bound reaction intermediates. *J. Phys. Chem. C* **2019**, *123*, 5951–5963.

[35] Ma, W. C.; Xie, S. J.; Liu, T. T.; Fan, Q. Y.; Ye, J. Y.; Sun, F. F.; Jiang, Z.; Zhang, Q. H.; Cheng, J.; Wang, Y. Electrocatalytic reduction of CO_2 to ethylene and ethanol through hydrogen-assisted C−C coupling over fluorine-modified copper. *Nat. Catal.* **2020**, *3*, 478–487.

[36] Mendieta-Reyes, N. E.; Cheuquepán, W.; Rodes, A.; Gómez, R. Spectroelectrochemical study of CO_2 reduction on TiO_2 electrodes in acetonitrile. *ACS Catal.* **2020**, *10*, 103–113.

[37] Cheng, H.; Liu, S.; Zhang, J. D.; Zhou, T. P.; Zhang, N.; Zheng, X. S.; Chu, W. S.; Hu, Z. P.; Wu, C. Z.; Xie, Y. Surface nitrogen-injection engineering for high formation rate of CO_2 reduction to formate. *Nano Lett.* **2020**, *20*, 6097–6103.

[38] Staszak-Jirkovský, J.; Malliakas, C. D.; Lopes, P. P.; Danilovic, N.; Kota, S. S.; Chang, K. C.; Genorio, B.; Strmcnik, D.; Stamenkovic, V. R.; Kanatzidis, M. G. et al. Design of active and stable Co-Mo-S_x chalcogels as pH-universal catalysts for the hydrogen evolution reaction. *Nat. Mater.* **2016**, *15*, 197–203.

[39] Yang, F.; Ma, X. Y.; Cai, W. B.; Song, P.; Xu, W. L. Nature of oxygen-containing groups on carbon for high-efficiency electrocatalytic CO_2 reduction reaction. *J. Am. Chem. Soc.* **2019**, *141*, 20451–20459.

[40] Guo, Y. B.; Chen, Q.; Nie, A. M.; Yang, H.; Wang, W. B.; Su, J. W.; Wang, S. Z.; Liu, Y. W.; Wang, S.; Li, H. Q. et al. 2D hybrid superlattice-based on-chip electrocatalytic microdevice for *in situ* revealing enhanced catalytic activity. *ACS Nano* **2020**, *14*, 1635–1644.

[41] Wang J. J., Wang G. J., Zhang J. F., Wang Y. D., Wu H., Zheng X. R., Ding J., Han X. P., Deng Y. D., Hu W. B. Inversely tuning the CO_2 electroreduction and hydrogen evolution activity on metal oxide via heteroatom doping. *Angew. Chem. Int. Ed.* **2021**, *60*, 7602–7606.